ACS OMEGA

http://pubs.acs.org/journal/acsodf

Article

Degradation-Dependent Controlled Delivery of Doxorubicin by Glyoxal Cross-Linked Magnetic and Porous Chitosan Microspheres

Nechikkottil Sivadasan Sumitha, Prabha Prakash, Balagopal N. Nair, and Gopalakrishnanchettiar Sivakamiammal Sailaja*

Cite This: *ACS Omega* 2021, 6, 21472−21484

Read Online

ACCESS | Metrics & More | Article Recommendations | Supporting Information

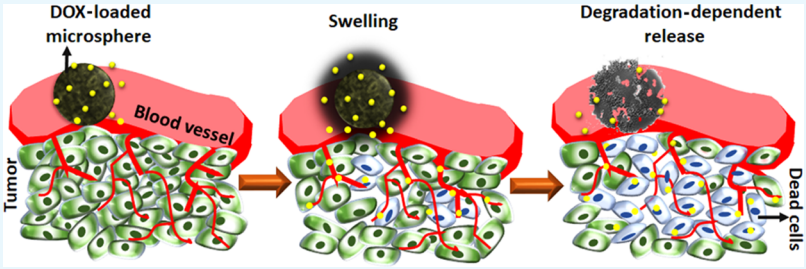

ABSTRACT: Glyoxal cross-linked porous magnetic chitosan microspheres, GMS (∼170 μm size), with a tunable degradation profile were synthesized by a water-in-oil emulsion technique to accomplish controlled delivery of doxorubicin (DOX), a chemotherapeutic drug, to ensure prolonged chemotherapeutic effects. The GMS exhibit superparamagnetism with saturation magnetization, M_s = 7.2 emu g^{-1}. The *in vitro* swelling and degradation results demonstrate that a swelling plateau of GMS is reached at 24 h, while degradation can be modulated to begin at 96−120 h by formulating the cross-linked network using glyoxal. MTT assay, live/dead staining, and F-actin staining (actin/DAPI) validated the cytocompatibility of GMS, which further assured good drug loading capacity (35.8%). The release mechanism has two stages, initiated by diffusion-inspired release of DOX through the swollen polymer network (72 h), which is followed by a disintegration-tuned release profile (>96 h) conferring GMS a potential candidate for DOX delivery.

INTRODUCTION

Clinical use of a large number of drugs is limited by their nonspecific uptake leading to reduced bioavailability, toxic side effects, and/or subsequent rapid elimination.[1−3] Controlled drug delivery systems are extensively investigated for appropriate drug release at the target site for a predefined period, to reduce the side effects associated with higher levels of drug consumption.[4−6] Further, implementation of such systems would also be beneficial to minimizing drug dosage/frequency to improve the therapeutic index. Polymer microspheres are widely employed as drug carriers/vehicles owing to their predominant therapeutic effect over traditional nascent forms of drugs.[6,7] Nevertheless, poor degradation of a majority of the polymers in biological milieu leads to long-term toxicity.[8]

The literature presents a wealth of information on the biomedical potential of chitosan, a biodegradable natural polymer, in the form of microspheres with regard to its excellent antibacterial property and tailored physicochemical and surface properties to enunciate regulated drug release in treating numerous diseases, including cancer.[6,9,10] In particular, specific targeting strategies of chitosan microspheres loaded with tumor-targeting drugs, *e.g.*, doxorubicin (DOX), 5-fluorouracil, *etc.*, significantly reduce the side effects of these drugs and enhance therapeutic efficiency.[6,11] In chitosan-based drug carriers, enhanced internalization by cells occurs by virtue of the electrostatic charge of amino groups in chitosan and facilitates a good endosomal escape ability.[12] In addition, chitosan renders opportunities for further functionalization, enabling ease of design and synthesis of multiresponsive therapeutic delivery agents based on chitosan and its derivatives.[13] The tethering of various targeting and therapeutic ligands imparts synergistic options for cancer therapeutics by offering better tumor inhibitory effects, less nonspecific distribution, and improved pharmacokinetics.[14−16] However, high solubility and lower mechanical strength of chitosan at lower pH environments (tumor analogous pH) necessitate modulation of its structure by appropriate cross-linking.[17]

Received: May 2, 2021
Accepted: July 30, 2021
Published: August 9, 2021

ACS Publications

© 2021 The Authors. Published by American Chemical Society

Scheme 1. Schematic Representation of the Synthesis of Glyoxal Cross-Linked Magnetic Chitosan Microspheres and Subsequent DOX Loading and Delivery

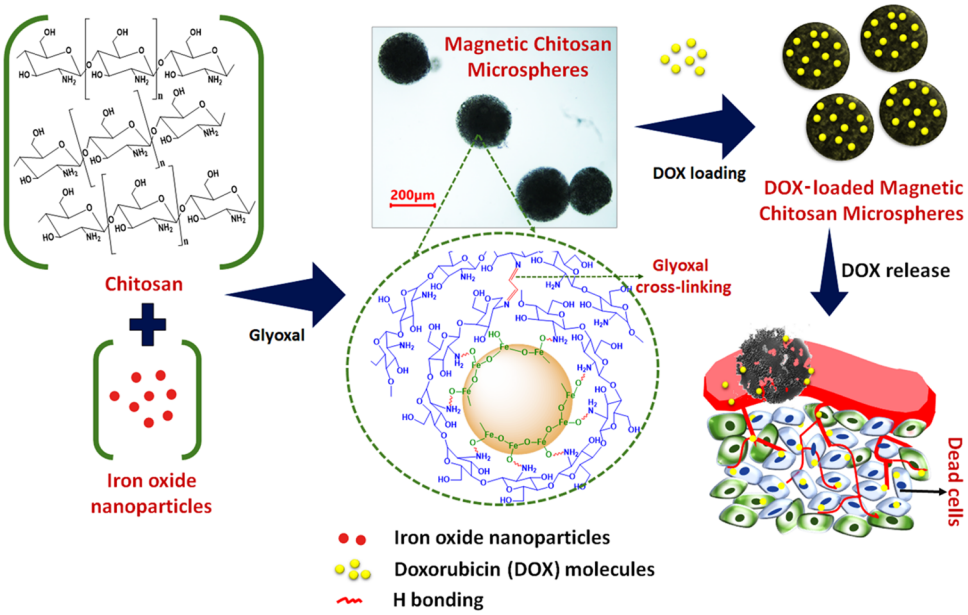

Conventional cross-linking agents such as glutaraldehyde induce irritation to mucous membranes, intraocular inflammation, *etc.* due to their inherent toxicity.[18,19] Therefore, it is highly desirable to identify a vital alternative cross-linker for chitosan microspheres, which is essentially cytocompatible. Glyoxal, a biocompatible dialdehyde, could be effective in cross-linking chitosan, *via* its aldehyde groups.[20] Wang and Stegemann have extensively studied the toxicity of glyoxal in terms of metabolic activity, viability, proliferation, and osteogenic differentiation of human bone marrow stem cells.[21] They have reported excellent biocompatibility of glyoxal even on direct exposure to cells for 15 h at a concentration of 1 mM.[21]

Advanced drug delivery options for cancer therapeutics avoid premature release of drugs at the extracellular level by employing multifunctional carrier systems. Multifunctional drug carriers are better particularly due to high loading capacity complemented with stimulus-responsive release kinetics such as temperature, pH, enzymes, photo conditions, magnetic/electric fields, *etc.*[4,5,10,22−25] The combined treatment methodologies like chemo-photodynamic therapy elicit synergistic effects at the tumor site, resulting in remarkable anticancer performance.[26−28] Recent applications proposed in theranostics include tumor microenvironment-responsive high-quality imaging in conjunction with drug release properties for oncotherapy.[28] Doping these nanocarriers with certain rare-earth metal ions imparts multimodal imaging potential, enabling image-guided treatment options. Besides this, incorporation of noble-metal nanoparticles such as Pt expedites deep tumor penetration through interaction with adherent junctions between cells and subsequent tumor ablation.[14] Among the several types of carriers, porous microspheres are especially attractive due to the capability of high loading efficiency offered by high surface area.[9−11]

Magnetically triggered drug release from polymer/nanoparticles has been widely accepted as both bioavailability and therapeutic efficacy can be tuned with better control due to intrinsic magnetic targeting.[5,25,29,30] Superparamagnetic materials are devoid of complications related to agglomeration, as they possess no net magnetic moment in the absence of an external magnetic field and hence are the most suited option for targeting purposes.[31] Superparamagnetic materials, particularly superparamagnetic iron oxide nanoparticles (SPIONs) with high magnetization, provide good dispersion stability and enable easy separation or targeting of the particles with the aid of an external magnetic field.[31] Beyond targeting, magnetic nanoparticle distribution in the polymer matrix offers additional advantages such as appropriate texture for the delivery system with increased surface roughness and hence high surface area to accommodate large quantities of drug molecules within the system and hence could be used for customized applications.[32]

Among the several chemotherapeutics used to treat different types of cancers, doxorubicin, an anthracycline drug, has shown very promising results and is widely used for the treatment of breast cancer, bladder cancer, lymphoma, acute lymphomatic leukemia, *etc.*[4,5,11,22] Nevertheless, the intravenous administration of DOX leads to severe toxic effects due to its indiscriminate distribution into undesired tissues and organs, especially the heart, liver, bone marrow, and skin.[33−35] The use of specific carriers for DOX and subsequent targeting to cancer sites not only declines its systemic toxicity but also improves its efficacy at lower doses, making the therapy more patient-friendly and cost-effective. Administration of drugs *via* biodegradable polymer-based delivery vehicles would be advantageous further by protecting the drug from degradation, in addition to sustained release through controlled degradation of the polymer inside the body to effectuate drug release.[9,18,25]

Here, degradation-responsive controlled release of DOX is presented *via* glyoxal cross-linked porous magnetic chitosan microspheres (GMS). GMS have been synthesized by an emulsion method by incorporating alanine-functionalized Fe_3O_4 (synthesized separately as per our previously reported procedure).[36] The alanine-functionalized Fe_3O_4 has high saturation magnetization and excellent biocompatibility. The physicochemical properties of GMS and control chitosan

https://doi.org/10.1021/acsomega.1c02303
ACS Omega 2021, 6, 21472−21484

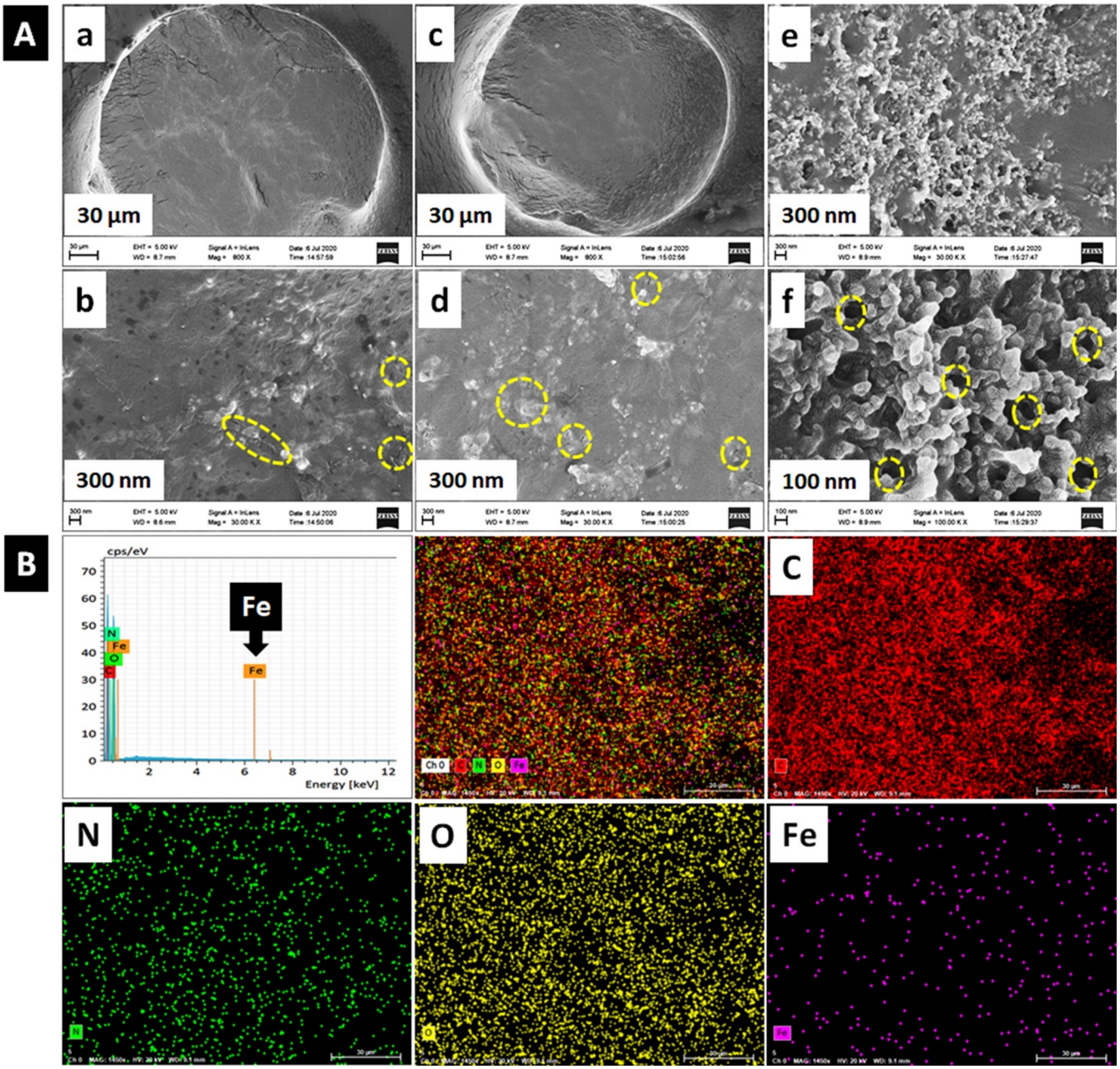

Figure 1. (A) FESEM images of microspheres. (a,b) CS; (c,d) GS; (e,f) GMS. (B) Energy-dispersive spectrum of GMS and elemental mapping showing the distribution of C, N, O, and Fe.

microspheres were investigated, which was followed by swelling and degradation and biocompatibility evaluation (MTT assay, live/dead assay, and cytoskeletal staining). The feasibility of GMS to be utilized as an effective drug delivery system has been validated by an *in vitro* release study by selecting DOX as the representative chemotherapeutic agent.

The synergistic functionalities, superparamagnetism, biocompatible cross-linking, and degradation-dependent drug release kinetics are noteworthy characteristics of GMS that allow favorable release of DOX for prolonged chemotherapeutic action. The mechanism hypothesized is that the initial release is triggered by swelling-assisted drug diffusion, which is followed by matrix degradation and erosion. GMS could therefore be proposed as an alternative to nonbiodegradable carrier systems such as polymethyl methacrylate microspheres and ethylene vinyl acetate-based drug carriers that need a second surgery to remove the carrier from the body after performing the desired function.[37−39]

■ RESULTS AND DISCUSSION

The schematic illustration of the synthesis of glyoxal cross-linked magnetic microspheres followed by DOX loading and delivery is represented in Scheme 1. The morphological evaluation of the noncross-linked, cross-linked, and magnetic samples by FESEM clearly indicates that the size, porosity, and exterior characteristics of the microspheres are largely influenced by the cross-linking and the dispersed magnetic content in the polymer matrix. The CS microspheres (Figure 1A a,b) are larger in size, having a 280 μm diameter, whereas GS (Figure 1A c,d) is viewed as slightly smaller in size, with a

https://doi.org/10.1021/acsomega.1c02303
ACS Omega 2021, 6, 21472−21484

diameter of 249 μm with a rougher surface texture enriched with numerous pores. The cross-linking of chitosan chains in the microspheres by glyoxal has resulted in size reduction. Gupta and Jabrail have reported consequences of cross-linking on the physical features of polymer products, where they have verified the size reduction by cross-linking as a result of compact arrangement of polymer chains occurring during the cross-linking reaction.[42] GMS (Supporting Information, Figure S1a,b) are featured with still lower size (~170 μm) and a highly porous structure with a slightly wrinkled surface (Figure 1A e,f). The exterior of the GMS contains microbump-like protrusions, which are clearly visible in the high-magnification image (Figure 1A f). The compactness of GMS is obviously due to the occupancy of A-IONP particles in the chitosan matrix, which might have interfered the cross-linking reaction and limited the number of interacting chitosan molecules to form bigger microspheres. Energy-dispersive spectroscopy and elemental mapping (Figure 1B) were employed to further identify the iron oxide distribution within the microspheres. Strong and homogeneous Fe signals were detected in the GMS microspheres (Figure 1B), indicating the successful incorporation and distribution of magnetic iron oxide nanoparticles in the whole matrix of GMS.

The surface characteristics, pore size, and pore size distribution are undeniably significant parameters in the design and development of microspheres. The well-defined spherical and highly porous morphology with a wrinkled surface is in favor of high loading capacity and controlled drug release. Based on the FESEM image, the size distribution of pores in GMS was determined using ImageJ software. It is shown in Figure 2 that the pore size of GMS falls in the range 35−160 nm with an average pore size of 75.5 nm.

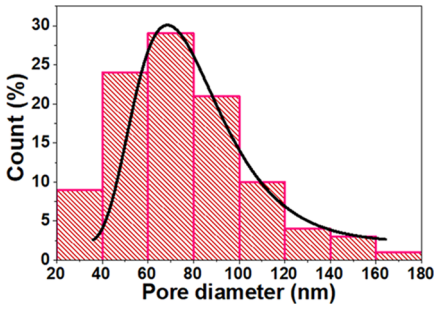

Figure 2. Pore size distribution curve of GMS calculated using ImageJ software.

The indication of Schiff base condensation, occurring between chitosan and glyoxal molecules during the cross-linking reaction, is perceived from FTIR spectra (Figure 3a). The peaks in the spectrum of CS are specified as follows: 3420 (N−H and O−H stretch), 2920 (CH_3 symmetric stretch), 1656 (C═O stretch of amide I), 1575 (NH_2 bend of amide II), 1427 (C−N stretch), 1380 (CH_3 symmetric deformation), 1260 (characteristic amide III stretching vibrations), and 1160 cm^{-1} (C−O−C bend).[43] After the cross-linking process, the carbonyl stretching of the amide I band shifted from 1656 to 1643 cm^{-1}, and the NH_2 bending of amide II has shifted from 1575 to 1554 cm^{-1} in GS, which is attributed to the stretching of the imine group (C═N) formed by nucleophilic attack of the nitrogen of the amino group (from chitosan) on the carbon of the glyoxal.[44,45] The distinctive absorption band at around 1069 cm^{-1} in the spectrum of GS results from the O−C−O

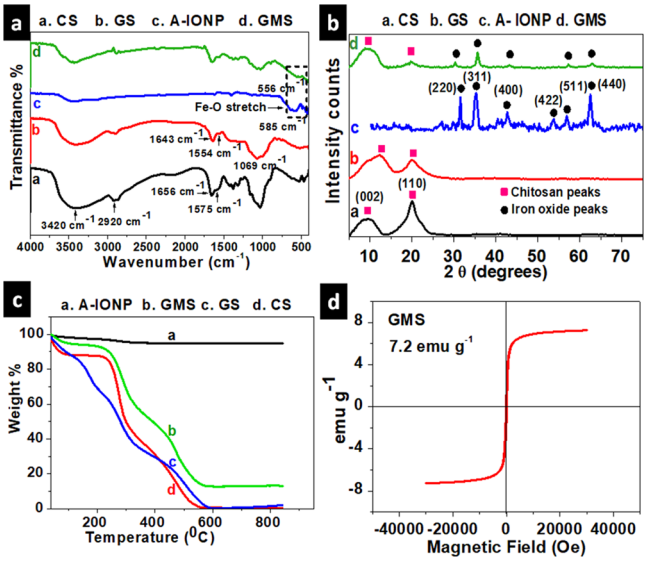

Figure 3. Structural, thermal, and magnetic properties of the microspheres: (a) FTIR spectra, (b) X-ray diffraction spectra, and (c) thermogravimetric profile of CS, GS, A-IONP, and GMS; (d) magnetization curve of GMS recorded at room temperature from −30,000 Oe to +30,000 Oe.

vibration attributed to acetalization between the hydroxyls of glucosamine in chitosan and the aldehyde group of glyoxal.[42,43,46] Acetalization and Schiff base formation have been further confirmed by the fact that the intensity of peaks in the range 1490−1220 cm^{-1} is reduced significantly in GS as compared to CS. Different types of Schiff base linkages can contribute biologically relevant properties such as tunable mechanical properties, chemical stability in physiological environments, and remarkable pH responsiveness, which collectively make this linkage of prime importance in biological applications, especially for drug delivery.[47−49]

A certain percentage of $-NH_2$ and −OH groups of chitosan has taken part in cross-linking, while the remaining groups are firmly bound to A-IONP, which is perceived from the shift of the Fe−O stretch to a lower wavenumber (556 cm^{-1}) in GMS compared to A-IONP (585 cm^{-1}).[50] Altogether, the magnetic particles strongly coexist with the polymer chains, which are interconnected through cross-linker molecules, forming a three-dimensional network structure capable of carrying the drug molecules.

CS shows diffraction peaks at 2θ = 10 and at 20° (Figure 3b) associated with the (002) and (110) planes of chitosan.[40,51] In GS, the intensity of the (002) plane has increased, while that of the (110) plane has diminished as a consequence of cross-linking. To acquire a better perception of the crystallinity of the samples, the percentage crystallinity was calculated at the respective crystalline peaks using eq 1, and the average was taken. Initially, the crystallinity of CS is relatively high (97.8%). The crystallinity at both characteristic peaks is reduced after cross-linking (to an average of 70.3%), which establishes evidence for the significant influence of cross-linking on the crystalline and amorphous properties of chitosan.[40] The structural sensitivity may be induced as a result of reorganizing the relative alignment of chitosan chains, attributable to the changes in hydrogen bonds of the chitosan network in the presence of cross-linking agents.[40,45] In CS, plenty of hydroxyl and amino groups could form strong

https://doi.org/10.1021/acsomega.1c02303
ACS Omega 2021, 6, 21472−21484

intermolecular and intramolecular hydrogen bonds to sustain certain regularity in the chitosan structure and high crystallinity thereof. The covalent cross-linking of chitosan chains in GS by glyoxal disturbs strong hydrogen bonds in the original chitosan, which thus interferes with the ordered packing of the chains and triggers the formation of amorphous regions.[45] This reduction in the crystallinity index of chitosan after cross-linking with glyoxal is already reported in the literature.[52] In the quantitative study of the crystalline structure of chitosan, Yang *et al.* found that glyoxal cross-linking instigated reduction of the crystal component of chitosan by 7.5%.[52]

The sharp, intense peaks of A-IONP are visible at 2θ values 30.0, 35.1, 42.9, 53.4, 57.0, and 62.6° equivalent to the reflections from planes (220), (311), (400), (422), (511), and (440), in the diffraction pattern of the magnetite phase of iron oxide (Figure 3b).[53] The diffraction planes corresponding to both GS and A-IONP are seen in GMS with less intense iron oxide peaks due to the interaction of these two phases.

Thermogravimetric analysis of the samples is illustrated in Figure 3c, and the derivative curves are given in Supporting Information, Figure S2. The samples CS and GS undergo stepwise weight losses in different temperature ranges. The first stage up to 120 °C, corresponding to a weight loss of 10−12%, is linked to desorption of physisorbed water on the samples.[54] Negligible degradation is observed for CS in the range 120−220 °C, and after that, a 61% weight loss occurs when the temperature reaches almost 370 °C. On the contrary, a dramatic weight loss process is noticed for GS up to 220 °C with the highest rate at 175 °C. It corresponds to a weight loss of 44% followed by a slightly lower degradation rate, which registers a weight loss of 68% at 370 °C. The weight loss in the range between 220 and 400 °C is caused by depolymerization of the polymer chains *via* the degradation of the glycosidic bonds.[45,54] This result implies that the thermal stability of GS is lower than that of CS at temperatures below 400 °C. The weight loss of GS is 32% higher than that of chitosan in the range 120−220 °C. This is because of the lower degree of crystallinity (by almost 27.5%) of GS as compared to CS, which is already evidenced from XRD analysis.

At higher temperatures (>400 °C), the thermogram of GS is shifted toward the right or higher temperature side owing to the high thermal stability. It is clear that the maximum degradation temperature in the last stage is 476 °C for CS and 513 °C for GS. The difference in the thermal degradation behavior at comparatively lower and higher temperatures can also be understood from the temperatures at which 50 ($T_{50\%}$) and 90% ($T_{90\%}$) degradation occurs for CS and GS. $T_{50\%}$ for CS and GS, respectively, are 299 and 278 °C, whereas $T_{90\%}$ are 492 and 524 °C (Supporting Information, Table S1). The last stage of thermal degradation, which occurs above 400 °C, corresponds to the thermal destruction of the pyranose ring of chitosan.[54] Results from this study indicate that though the breakage of the main chain occurs much faster in GS, it is more stable in the glucose units under high temperature compared to CS.[45] The thermogram of magnetic microspheres also presents this shift coupled with a higher remnant weight of 12.8% at 800 °C. The higher thermal stability of GS at higher temperature is ascribed to cross-linking between chitosan chains by glyoxal, and that of GMS results from the synergistic effect of cross-linking and the presence of magnetic nanoparticles.

It is highly noteworthy mentioning that the GMS microspheres inherited magnetic characteristics of A-IONP (Supporting Information, Figure S3, M_s = 56 emu g^{-1}) and possess superparamagnetism (Figure 3d, M_s = 7.2 emu g^{-1}). The magnetic shielding effect of a higher amount of nonmagnetic chitosan in GMS leads to its attenuated M_s value. The same observation was reported by Jianmei *et al.* by studying the polymer/Fe_3O_4 ratio-dependent change in magnetic saturation.[55] In the Fe_3O_4@polyvinyl alcohol microspheres prepared by them, the M_s value reached up to 15 emu g^{-1} when the Fe_3O_4 content was 33.3%, while the M_s value was <10 when Fe_3O_4 was 20%.[55] Similar results were reported by Rodkate and Rutnakornpituk for the carboxymethyl chitosan-based magnetic hydrogels having M_s value of 3.6 emu g^{-1} (<20% magnetic content).[56] Superparamagnetism is a preferred choice for targeted drug delivery systems, microspheres, and other biomedical applications on account of the nonretaining of magnetism in the absence of an external magnetic field. The glyoxal cross-linked magnetic chitosan microspheres presented have been validated for their physicochemical (FTIR, XRD, and TGA) and magnetic characteristics.

The drug loading and subsequent release profile of porous materials are profoundly guided by the degree of swelling. With an increase in the swelling index, the mobility of polymer chains increases, and therefore, the free volume available for diffusion of encased drug molecules increases. The swelling studies were performed at two pH conditions, pH 7.4 (physiological pH) and pH 5.6 (corresponding to the tumor microenvironment). The microspheres exhibit pH-responsive swelling behavior as viewed from Figure 4a,b. Figure 4a shows the swelling index of microspheres in PBS (pH 7.4), which demonstrates that they exhibit an ability to absorb large amounts of the solvent. The cross-linking and the amount of

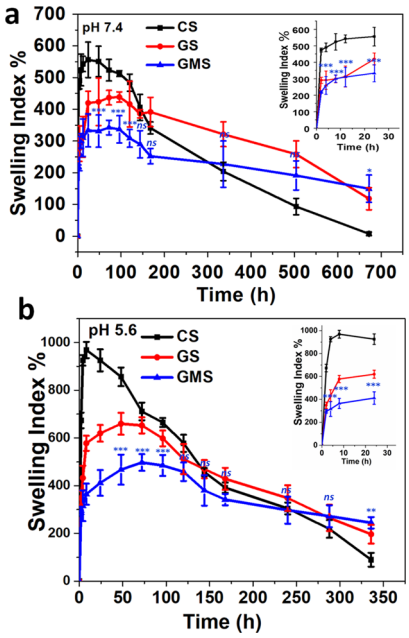

Figure 4. Swelling index of CS, GS, and GMS (a) in phosphate-buffered saline (1 M, pH 7.4) and (b) in acetate buffer (0.1 M, pH 5.6). Note: values are presented as mean ± standard deviation. "ns" indicates nonsignificance ($p > 0.05$), while "*" ($p < 0.05$), "**" ($p < 0.01$), and "***" ($p < 0.001$) indicate statistical significance (comparison of the swelling index of GMS with that of the control sample, CS).

https://doi.org/10.1021/acsomega.1c02303
ACS Omega 2021, 6, 21472−21484

dispersed magnetic particles in the polymer matrix have a strong influence on the swelling degree. Chitosan contains abundant hydroxyl and amino groups so that it is quickly hydrated. After cross-linking, the amount of hydrophilic groups in the chitosan chains decreases, and it exhibits a lesser degree of water absorption in buffer solution. The lowering of the swelling index of the chitosan matrix due to the increased polymer density after cross-linking reactions has already been reported by several researchers.[57] The CS microspheres reach a saturated swelling degree of about 554% within a period of 12 h, while for GS and GMS, it took 24 h to reach the saturation at pH 7.4. The swelling index of both GS and GMS is lower than that of CS. In GS, the cross-linked chitosan network limits the entry of water molecules into the microspheres as compared to CS, while in GMS, the magnetic particles dispersed among the polymer chains interrupt the penetration of water molecules through the polymer network. After attaining saturation, the swelling index of the samples remains constant, and thus, the graphs run almost parallel to the *X* axis (24−96 h). Overall, the swelling profile shows three stages, including the rapid initial stage of saturation, a plateau (second stage), and the third stage that corresponds to the degradation of the matrix. The degradation of CS starts at 72 h, whereas that of GS starts at >96 h indicating the enhanced stabilization of cross-linked microspheres in the physiological medium. Degradation of GMS also begins at 96−120 h. Analyzing the third stage of the swelling profile, it is apparent that the rate of degradation of CS is quicker, while those of GS and GMS occur by taking a comparatively longer time. As the swelling index of CS is very high, the molecules move apart by holding water inside the network that in effect enables rapid degradation of the sample. As the swollen particles of CS are heavier, the stress exerted on the particles in bottom layers will be higher. This also could lead to faster degradation.

The mechanism of swelling of microspheres in physiological pH was studied by fitting the obtained experimental data with first-order and second-order kinetic equations. The corresponding plots and results are respectively displayed in Figure S4 and Table 1. From the comparison of the obtained correlation coefficients (R^2) for each swelling kinetic model, it is understood that for all the samples, the swelling kinetics are best fitted with the second-order kinetic model. Further, it conveys that the entire swelling process is primarily controlled by two factors: the initial rate of swelling and equilibrium swelling, respectively.[41,58]

Table 1. Correlation Coefficient (R^2) Values Corresponding to Fitting of Swelling with First-Order and Second-Order Kinetic Equations

	R^2 value	
sample	first order	second order
CS	0.8964	0.9987
GS	0.9533	0.9995
GMS	0.7549	0.9996

Figure 4b represents the swelling index of CS, GS, and GMS at pH 5.6. There is a substantial enhancement in the swelling index in pH 5.6 when compared to that in pH 7.4, for all the samples. At pH 5.6, the amino groups in chitosan are in a protonated state, which makes the matrix more hydrophilic to absorb more water molecules compared to pH 7.4, where the protonation is not much significant. At pH 7.4, there are not enough protons to produce positive charges in chitosan. It leads to fast achievement of equilibrium swelling of CS (almost 85% higher within 8 h) in pH 5.6 than in physiological pH. Similar to the swelling in pH 7.4, CS exhibits a higher swelling index, which is followed by GS and GMS, indicating that both cross-linking and incorporation of A-IONP are two key parameters that influence the swelling degree. When glyoxal molecules cross-link the amino groups of chitosan, the free amino groups of GS (to be protonated in an acidic medium) decrease. In addition, the cross-linked network minimizes the mobility of polymer chains. These factors together lead to lower swelling of GS. On the contrary, the macromolecular chains of CS could expand better, resulting in a faster degradation (begins at 24 h); the swollen microspheres lose mechanical integrity leading to erosion and disintegration of the polymer. Moreover, GMS exhibited the lowest swelling (454%) and a delayed onset of degradation (begins at >120 h), owing to the compact structure originating from cross-linking and A-IONP loading. The pH-responsive swelling and better expanded nature of the microspheres in acidic pH lead to effective tumor-specific drug release.

The partially disintegrated microstructure of GMS after one-month degradation in PBS is given in Figure 5a,b. With the formation of cavities or channels, the internal structure becomes unstable, resulting in cracks emerging in these microspheres.[59,60] The loss of structural integrity gives rise to disintegration of the matrix, which in turn facilitates release of loaded drug molecules. It should be noted that no leaching out of magnetic particles from GMS is observed even after one-month swelling studies in PBS. If there is no binding between A-IONP and chitosan, all the magnetic particles would have leached out when they come immediately in contact with the medium. Conversely, the long-drawn-out degradation and the absence of any leaching out establishes a fairly good binding between the magnetic particles and the polymer matrix, which in turn would lead to favorable physiological functions.

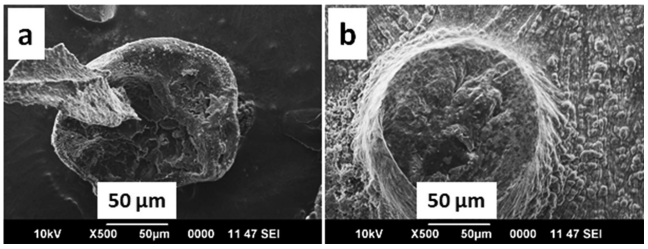

Figure 5. (a,b) SEM micrographs demonstrating the disrupted morphology of GMS after one month degradation in 1 M phosphate-buffered saline, pH 7.4.

An appropriate degradation profile of a drug carrier would become appreciably effective when it is biocompatible. The cell viability of microspheres was assessed by MTT assay (Figure 6) at two time points (day 1 and day 5) using different concentrations of microsphere extracts (50−200 μg mL^{-1}) and is represented in terms of absorbance values. It could be viewed that for all samples at 50 μg mL^{-1} concentration, the absorbance has increased significantly from day 1 to day 5, which is comparable to that of control cells. Increased absorbance values show cell proliferation. The results therefore indicate good cytocompatibility of the microspheres, reflecting the cell viability as a function of mitochondrial activity in living cells. It is to be noted that there is no statistically significant

https://doi.org/10.1021/acsomega.1c02303
ACS Omega 2021, 6, 21472−21484

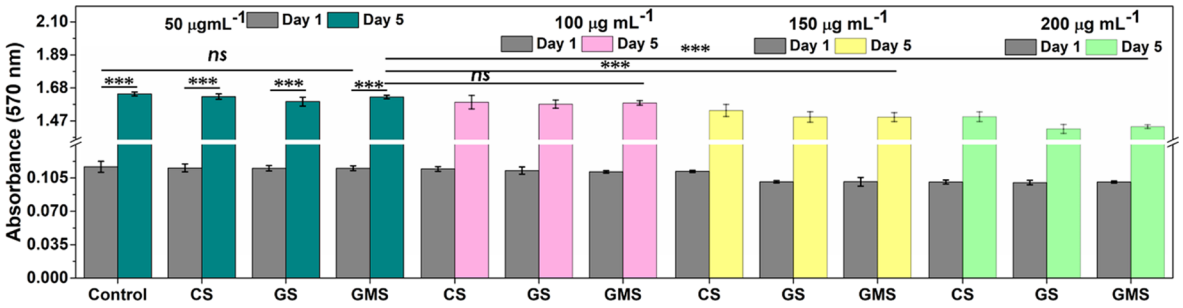

Figure 6. Cell viability of control cells, CS, GS, and GMS by MTT assay at 50, 100, 150, and 200 μg mL^{-1} sample concentrations at two time points, day 1 and day 5. Note: values are presented as mean ± standard deviation. "ns" indicates nonsignificance ($p > 0.05$), while "*" ($p < 0.05$), "**" ($p < 0.01$) and "***" ($p < 0.001$) indicate statistical significance.

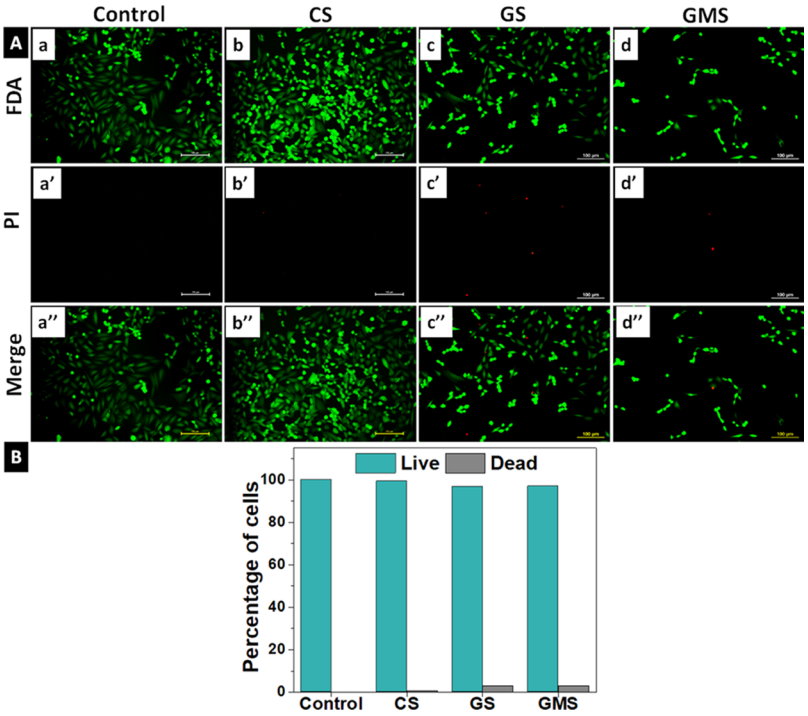

Figure 7. (A) Live/dead imaging of control cells (a−a″), cells treated with CS (b−b″), GS (c−c″), and GMS (d−d″) at 50 μg mL^{-1} concentration for 24 h, with a scale bar of 100 μm; (B) percentage of live and dead cells calculated from live/dead imaging.

reduction in cell viability up to 100 μg mL^{-1} sample concentration. However, beyond that concentration, the cell viability and proliferation were slightly affected by the microspheres, as compared to control cells, though an increase in the proliferation index results on day 5 compared to day 1.

Figure 7A shows the fluorescence images of cells based on live/dead assay in order to assess the viability of HOS cells treated with samples (50 μg mL^{-1} concentration) for 24 h. The simultaneous use of two dyes, fluorescein diacetate (FDA) and propidium iodide (PI), which stain live cells and dead cells, respectively, allows the distinction of live cell population from the population of dead cells. FDA is taken up by live cells, which convert the nonfluorescent FDA into the green fluorescent metabolite fluorescein, and the measured signal serves as an indicator for viable cells. In contrast, the nucleus-staining dye PI cannot pass through a viable cell membrane.[61] It passes through disordered areas of dead cell membranes, reaches the nucleus, and intercalates with the deoxyribonucleic acid (DNA) double helix. High numbers of live cells were noticed on all the samples. Figure 7B shows the percentage of live cells after being quantified from the fluorescence images. The quantitative data provides a comparative study of the biocompatibility of the three microspheres, which together with MTT assay results demonstrate excellent biocompatibility of the microspheres.

The distinct filamentous cytoskeleton of a cell is involved in several cytoplasmic and nuclear functions.[62,63] It is therefore of considerable interest to investigate the distribution of actin filaments of cells after treating with samples, as it affords direct information on actin structures in particular and overall cell morphology in general, reflecting the cell-material interactions. The cell cytoskeleton images (Figure 8b−b″, c−c″, and d−d″) suggest that none of the samples induced alterations of actin microfilaments/nuclear structure or the cytoskeleton organization and are comparable to untreated (control) cells (Figure 8a−a″), further evidencing cytocompatibility of the microspheres.

The release of DOX from DOX-loaded GMS was confirmed by the drug release profile (Figure 10b,c) where 13.5% DOX release occurred within 24 h. In order to analyze the effect of

https://doi.org/10.1021/acsomega.1c02303
ACS Omega 2021, 6, 21472−21484

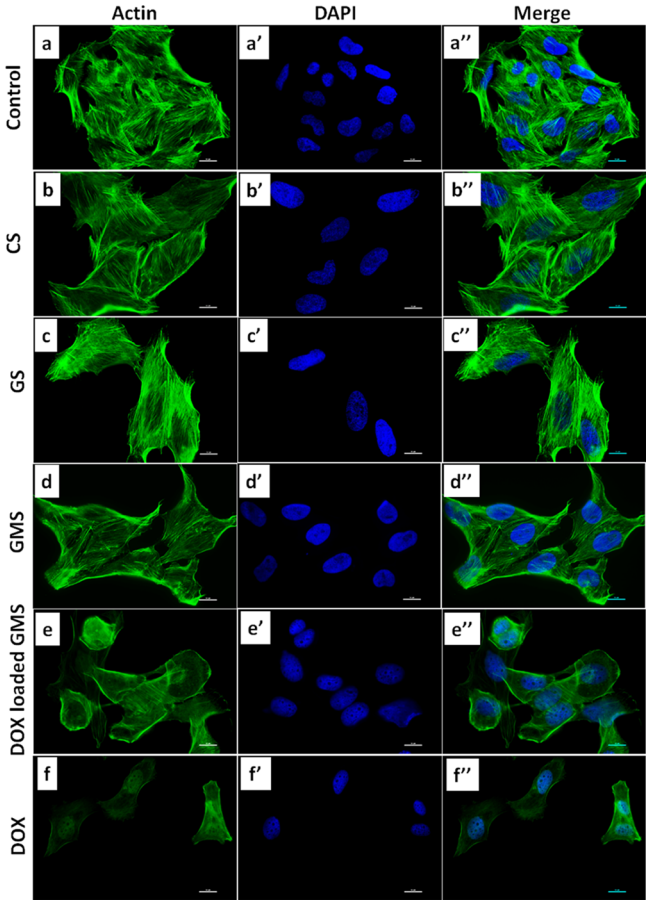

Figure 8. Cell cytoskeleton images of (a–a″) control cells and cells treated with (b–b″) CS, (c–c″) GS, (d–d″) GMS, and (e–e″) DOX-loaded GMS at 50 μg mL^{-1} concentration and (f–f″) DOX at 35.8 μg mL^{-1} concentration for 24 h. Actin filaments were stained with Alexa Fluor-488 and nuclei with DAPI, with a scale bar of 10 μm.

released DOX, the samples were incubated with HOS cells for 24 h, and the cytotoxic effect of DOX released from DOX-loaded GMS was assessed (Figure 8e–e″) and compared with control (untreated) cells (Figure 8a–a″) as well as free DOX-treated cells (Figure 8f–f″). It is obvious that the released DOX could interact with cells and induce morphological alterations.

The time- and concentration-dependent cytotoxic response of released DOX was studied further by MTT assay. Figure 9A shows MTT assay results of cells treated with DOX-loaded GMS and DOX, which elicited significant cytotoxic effects within 24 h, as viewed from the reduced absorbance values compared to the cell viability of control cells. Further, the live cell population is remarkably reduced from day 1 to day 5, demonstrating a decrease in cell viability as a function of DOX release. The drug release potential of DOX-loaded GMS was also confirmed by live/dead staining (Figure 9), where an increased percentage of dead cell population is visible for the DOX-loaded GMS (Figure 9B a–a″) and DOX (Figure 9B b–b″) compared to control cells (Figure 7a–a″). Estimated percentages of live and dead cells are presented in Figure 9C, where substantial toxicity levels arise as a result of time-dependent release of DOX from the microspheres. As a result, the cell signaling and motility are destroyed, ultimately leading to the annihilation of tumor cells.

The drug loading and release studies of GMS and GS microspheres are compared by selecting DOX as the model chemotherapeutic drug. GMS exhibit a higher loading capacity (35.8%) than GS microspheres (21.5%) (Figure 10a). This is probably due to the wrinkled and porous texture of GMS, offering it a high surface area to volume ratio. In clinical therapeutics, it is necessary to maintain the drug at a therapeutic serum concentration for a specific period of time. Thus, the microspheres with a minimal initial burst release and a relatively well-controlled sustained release are likely to be ideal drug carriers.

The DOX release behavior in acetate buffer at pH 5.6 is shown in Figure 10b,c. The initial release (up to 8 h) is slightly higher (by ∼3.1%) for GMS because of the relatively rapid diffusion of the physically entrapped drug molecules from the highly porous exterior (Figure 10b). This initial burst is followed by a slow release up to about 120–144 h (31%), and after that, a sudden increased release at 168 h (48%) was observed. This could be correlated with the swelling profile where degradation of GMS begins at >120 h. For GS, the initial release is lower; later on, faster release than GMS was found since the elevated swelling index of GS permits the embedded drug molecules to diffuse out in to the medium. Thus, the morphological and swelling characteristics of the carrier matrices are reflected in the drug release profile. The long-term release studies show the long-term drug retention of the samples and sustained release in the mimicked tumor environment. The higher rate of degradation of GS compared to GMS was accompanied by a loss of integrity of their structures leading to the formation of cavities or channels across the matrix, which enhance the rate of drug release.

In this study, we have developed biocompatible, magnetic, and porous chitosan microspheres as a long-term controlled drug delivery system in which the drug release is triggered initially by diffusion and later by degradation of the polymer matrix, validated using DOX as the model drug. It is well-known that chitosan is a widely used biopolymer for a variety of applications in the biomedical field.[64,65] As a promising biodegradable material, the rapid rate of degradation and loss of structural integrity of chitosan in an aqueous medium limit its further applications.[66,67] To overcome these challenges, cross-linking and magnetic modulation were adopted to tune the size, surface morphology, swelling, and degradation profile to impart favorable features for controlled drug release.[68] Both cross-linking and magnetism play key functions in tailoring the drug release rate.[56] It is known that drug release from microspheres depends both on drug diffusion through the polymer matrix and on polymer degradation.[60] In the initial stage of release, the exposed drug molecules on and near the exterior of the microspheres would diffuse out into the medium. During the degradation period *in vitro*, the swelling index reaches a maximum; subsequently, pores and cracks appear on the surface of microspheres, extending inside due to disentanglement of chitosan chains in the medium. Thus, the medium (buffer) can easily penetrate into the microspheres and bring out the drug molecules encapsulated inside. Finally, when disintegration begins, numerous pores, cavities, and channels are formed inside the microspheres, and the drug can diffuse out of the microspheres through this deformed structure.[69]

https://doi.org/10.1021/acsomega.1c02303
ACS Omega 2021, 6, 21472–21484

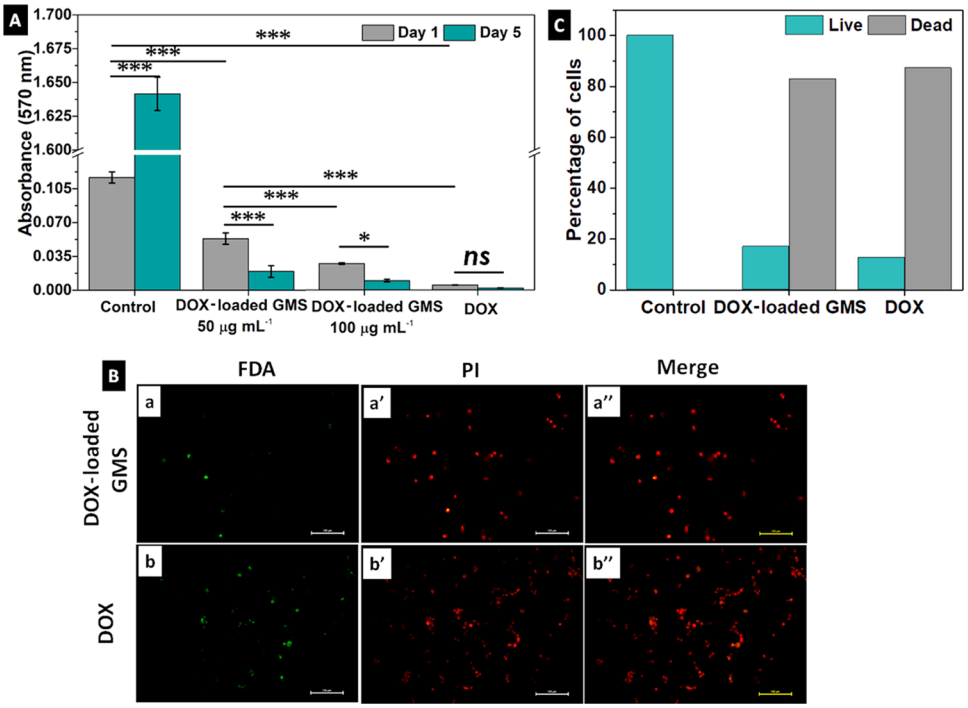

Figure 9. (A) Cell viability of control cells, DOX-loaded GMS (at 50 and 100 μg mL^{-1} sample concentrations), and DOX (35.8 μg mL^{-1}) by MTT assay at two time points, day 1 and day 5. (B) Live/dead imaging of cells treated with (a−a″) DOX-loaded GMS at 50 μg mL^{-1} and (b−b″) DOX at 35.8 μg mL^{-1} concentration for 24 h, with a scale bar of 100 μm. (C) Percentage of live and dead cells calculated from live/dead imaging. Note: values are presented as mean ± standard deviation. "ns" indicates nonsignificance ($p > 0.05$), while "*" ($p < 0.05$), "**" ($p < 0.01$), and "***" ($p < 0.001$) indicate statistical significance.

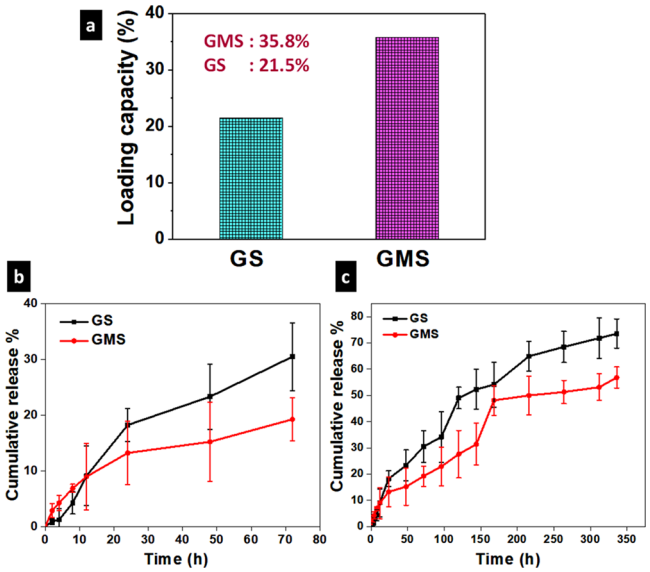

Figure 10. Drug loading and release kinetics of microspheres: (a) drug loading capacity of GS and GMS; (b) short-term drug release up to 72 h at pH 5.6; (c) long-term drug release up to 14 days, pH = 5.6.

CONCLUSIONS

In summary, porous, glyoxal cross-linked magnetic microspheres of chitosan (GMS) with controlled DOX delivery were developed by an emulsion cross-linking technique for cancer chemotherapy, which enable customized degradation of the drug delivery matrix as a function of the degree of cross-linking by a biocompatible cross-linker, glyoxal and A-IONP contents. The structure, cytocompatibility, *in vitro* degradation, and drug release profile of the microspheres were evaluated. GMS have a distinguished combination of functionalities, a controllable swelling index, a high loading capacity, and a long-term controlled drug release. The DOX-loaded GMS induced substantial cytotoxicity under *in vitro* conditions due to time-dependent DOX release. The drug release behavior is controlled initially by diffusion and swelling and later by matrix degradation, presenting these magnetic microspheres as drug delivery platforms to replace nondegradable polymeric carriers.

EXPERIMENTAL SECTION

Materials. Chitosan (degree of deacetylation ≥ 75%) was obtained from Sigma Aldrich. NaCl, glacial acetic acid, paraffin liquid heavy, petroleum benzine (60−80 °C), NaOH, $NaBH_4$, and 25% ammonia were supplied by Merck Life Sciences Pvt. Ltd., Mumbai, India. $FeCl_3{\cdot}6H_2O$ was purchased from Loba Chemie Pvt. Ltd., Mumbai, India. Alanine and 40% glyoxal were procured from Spectrochem Pvt. Ltd., Mumbai, India. Milli-Q water with a specific resistance of 18.2 MΩ cm (from Merck Millipore) was used throughout the experiment.

Synthesis of Alanine-Functionalized Iron Oxide Nanoparticles (A-IONP). Alanine-functionalized IONP were synthesized as reported elsewhere.[36] Briefly, an $FeCl_3{\cdot}6H_2O$ solution was complexed with DL alanine in the Fe/alanine molar ratio 1:0.1 in an aqueous medium under a N_2 atmosphere at room temperature. The complexed Fe^{3+} was subjected to reduction with the aid of 224 mM $NaBH_4$ followed by oxidation using a 25% ammonia solution to yield alanine-functionalized Fe_3O_4 nanoparticles. The sample was collected by means of a magnetic field and washed to neutral pH using Milli-Q water and named as A-IONP.

https://doi.org/10.1021/acsomega.1c02303
ACS Omega 2021, 6, 21472−21484

Synthesis of Microspheres. Chitosan (2% (w/v)) in glacial acetic acid was used for microsphere synthesis. It was done by a water-in-oil emulsion method at a temperature of 55 °C using paraffin liquid-petroleum benzine as the oil phase and polyvinyl alcohol (PVA) (2% (w/v)) as the suspending agent in the presence of 4 N NaOH. Post-synthesis cross-linking with glyoxal was done using a 2% glyoxal solution at pH 4 for 2 h at room temperature. The synthesized samples were washed subsequently with petroleum benzine, ethanol, and Milli-Q water. The microspheres were dried by lyophilization for 72 h. The noncross-linked microspheres are named as CS, while glyoxal cross-linked microspheres are named as GS. The synthesis of magnetic chitosan microspheres was performed by following the same procedure as that of CS. Instead of a chitosan solution, chitosan/A-IONP in an 80:20 (w/w) ratio has been taken, and subsequently, the magnetic microspheres are named as GMS.

Physicochemical Characterization. The infrared spectra were collected on a Fourier transform infrared (FTIR) spectrometer (PerkinElmer, U.K.) by transmittance mode (4000−400 cm^{-1}). The phase composition and crystallinity of iron oxide and microsphere samples were analyzed by X-ray diffraction (XRD) (Bruker AXS D8 Advance X-ray diffractometer) through the 2θ range from 5 to 75° at a step size of 0.02°. The crystallinity index (CI) was calculated using the following equation[40]

$$\mathrm{CI}\ \% = \frac{(I_0 - I_{\mathrm{am}})}{I_{\mathrm{o}}} \times 100 \tag{1}$$

where I_{o} is the maximum intensity and I_{am} is the intensity at amorphous diffraction.

Thermal stability under a N_2 environment was determined using a TA Q 50 thermogravimetric analyzer (TGA) by heating from 40 to 800 °C at a rate of 20 °C min^{-1}, and surface morphologies were analyzed using a JEOL Model JSM-6390LV scanning electron microscope. Field-emission scanning electron microscopy (FESEM) characterization of the microspheres was done in ZEISS, SIGMA (Germany). Magnetic response curves of the samples were recorded in the Physical Property Measurement System (PPMS), Quantum Design Dynacool, at room temperature.

The swelling behavior was studied by immersing 2 mg of microspheres in phosphate-buffered saline (PBS) solution (1 M, pH 7.4) and in acetate buffer (0.1 M, pH 5.6) and shaking at 55 rpm at 37 °C (triplicate). The swollen weight of the microspheres was taken at predetermined time intervals, and the degree of swelling was calculated using the following equation

$$\text{Swelling Index}(\%) = \frac{(W_t - W_0)}{W_0} \times 100 \tag{2}$$

where W_t represents the weight of the swollen sample at time "t" and W_0 is the weight of the dry sample. To simulate the flow of the biological liquid, the buffer solution was replaced at every 24 h. The possibility that the swelling follows first-order or second-order kinetics has been found out using first-order and second-order equations[41] by taking the swelling index values in the initial stage (up to maximum uptake). According to first-order kinetics, the rate of swelling at any given time, t, is directly proportional to the uptake of the swelling medium that has yet to occur before the maximum or equilibrium uptake (W_∞) is reached. The following equation represents this relation

$$\frac{\mathrm{d}\,W_t}{\mathrm{d}\,t} = k(W_\infty - W_t) \tag{3}$$

where W_t is the uptake at time t, $W_\infty - W_t$ is the unrealized uptake of the swelling medium, and k is the proportionality constant. This can be integrated into

$$\ln\left(\frac{W_\infty}{W_\infty - W_t}\right) = kt \tag{4}$$

Further, the second-order kinetics can be represented by the following equation

$$\frac{t}{W_t} = A + \frac{t}{W_\infty} \tag{5}$$

where A is constant.

Cell Culture. The human osteosarcoma (HOS) cell line was purchased from the National Centre for Cell Science (NCCS), Pune, India and cultured in Dulbecco's modified Eagle medium (DMEM, high glucose, Gibco, Thermo Fischer Scientific, India) supplemented with 4% fetal bovine serum (FBS, Gibco, Thermo Fischer Scientific, India) and a 1% antibiotic solution containing penicillin and streptomycin (Sigma Aldrich, USA) at 37 °C in a 5% CO_2 incubator.

MTT Assay. Cell viability of the microspheres was evaluated using an MTT [3-(4,5-dimethylthiazol-2-yl)-2,5-diphenyltetrazolium bromide] assay at two time points (day 1 and day 5). For this, the extracts of microspheres were taken by stirring 10 mg of the sample in 10 mL of water at 37 °C for 48 h. The HOS cells (~3×10^3) were seeded into each well of a 96-well cell culture plate and incubated for 24 h in a CO_2 incubator at 37 °C followed by the addition of extracts of microspheres: CS, GS, GMS (50, 100, 150, and 200 μg mL^{-1} concentrations), DOX-loaded GMS (50 and 100 μg mL^{-1} concentrations), and free DOX (at 35.8 μg mL^{-1} concentration corresponding to the amount of the drug in DOX-loaded GMS). On the first and fifth day of incubation, the culture medium was pipetted out and replaced with 20 μL MTT (5 mg mL^{-1} in PBS, 1 M, pH 7.4) and incubated in the dark. Over 4 h of incubation, insoluble purple formazan crystals were formed, which were then solubilized in dimethyl sulfoxide (100 μL). The absorbance was recorded at 570 nm in a multiwell microplate reader (Spark Multimode Microplate Reader, Tecan, Switzerland).

Live/Dead Imaging. Live/dead imaging was performed after 24 h of incubation of HOS cells with the samples at a concentration of 50 μg mL^{-1}. HOS cells were seeded at a density of 3×10^3 cells/well in a 24-well adherent plate and incubated with CS, GS, GMS, DOX-loaded GMS, and DOX (at a concentration equivalent to the loaded amount in GMS, 35.8 μg mL^{-1}) for 24 h. Approximately 300 μL of fluorescein diacetate (FDA; stock solution of 5 mg mL^{-1} prepared in acetone, which is diluted in an incomplete medium at a 1:500 ratio) solution was added to each well followed by the addition of 2 μL of propidium iodide (PI, 1:100 dilution in an incomplete medium) solution, after 10 min of incubation. Again after 1−2 min of incubation, the cells were observed under a Nikon-Ti20 microscope.

Cytoskeleton Staining. HOS cells (3×10^3) were seeded in surface-treated cover slips in a 24-well plate and incubated for 24 h at 37 °C and 5% CO_2. The samples (CS, GS, GMS,

https://doi.org/10.1021/acsomega.1c02303
ACS Omega 2021, 6, 21472−21484

and DOX-loaded GMS) were added at a concentration of 50 μg mL^{-1} in triplicate. After 24 h of incubation, the medium was removed, and the cells were fixed using a 4% paraformaldehyde solution (in PBS 1×, pH = 7.4). The fixative was removed after 10 min of incubation followed by careful washing thrice with PBS. After permeabilization of the cells with 50% ice-cold methanol for 10 min, 2% bovine serum albumin (BSA) was added, and the cells were kept at room temperature for 20 min. Then, 100 μL of the Alexa Fluor-488 primary antibody prepared in BSA (1:100 dilution) was added followed by incubation for 30 min at room temperature. The unincorporated dye was removed, and the nuclei were counterstained with 4′,6-diamino-2-phenylindole (DAPI, 3 nM in PBS). The cells were then washed with PBS and observed under a fluorescence microscope (Nikon-Ti20). The excitation/emission wavelengths for Alexa Fluor-488 and DAPI are 493/519 and 358/461 nm, respectively.

Drug Loading and *In Vitro* Drug Release Studies. The microspheres (10 mg) were added into 100 mL of doxorubicin solution (0.1 mg mL^{-1}) and shaken at 37 °C for 48 h in an incubator shaker at 55 rpm. The microspheres were collected from the drug solution, and the loading capacity was calculated using the difference in the absorbance values of the drug solution before and after drug loading experiments at 480 nm. Values of drug concentration were obtained from the calibration curve, which was determined by taking absorbance vs doxorubicin concentration. The drug loading capacity was calculated using the following equation

$$\text{Drug loading capacity}(\%) = \frac{(C_0 - C_t) \times V}{C_0 \times M} \times 100 \quad (6)$$

where C_0 is the initial and C_t is the final concentrations of the drug solution. V is the volume of the drug solution, and M is the mass of the microspheres.

The release behavior was studied by immersing 5 mg of microspheres in 10 mL of acetate buffer (pH 5.6) at 37 °C and stirring at 55 rpm. At predetermined time intervals, 200 μL of the release medium from each sample was withdrawn; then, an equal volume of fresh buffer was added immediately. The doxorubicin concentration was determined by UV−visible spectroscopy. The cumulative release (%) was plotted against time.

Statistical Analysis. All the values are presented as mean ± standard deviation. The level of statistical significance was measured by Tukey's multiple comparison tests using GraphPad Instat3 software.

■ ASSOCIATED CONTENT

Supporting Information

The Supporting Information is available free of charge at https://pubs.acs.org/doi/10.1021/acsomega.1c02303.

FESEM images of GMS, DTG curves, magnetization curve of A-IONP, and swelling kinetics (PDF)

■ AUTHOR INFORMATION

Corresponding Author

Gopalakrishnanchettiar Sivakamiammal Sailaja − *Department of Polymer Science and Rubber Technology, Inter University Centre for Nanomaterials and Devices (IUCND), and Centre for Excellence in Advanced Materials, Cochin University of Science and Technology, Kochi 682 022 Kerala, India;* orcid.org/0000-0002-6406-7293; Phone: +91-9744799643; Email: sailajags@cusat.ac.in

Authors

Nechikkottil Sivadasan Sumitha − *Department of Polymer Science and Rubber Technology, Cochin University of Science and Technology, Kochi 682 022 Kerala, India*

Prabha Prakash − *Department of Biotechnology, Cochin University of Science and Technology, Kochi 682 022 Kerala, India*

Balagopal N. Nair − *School of Molecular and Life Sciences (MLS), Faculty of Science and Engineering, Curtin University, Perth WA6845, Australia*

Complete contact information is available at: https://pubs.acs.org/10.1021/acsomega.1c02303

Author Contributions

N.S.S. has conducted the experiments and analysis and interpretation of data and also written the draft. P.P. has performed the cell culture experiments. G.S.S. has conceptualized the idea, supervised the work, and edited the manuscript. B.N.N. has provided overall guidance and edited the manuscript.

Notes

The authors declare no competing financial interest.

■ ACKNOWLEDGMENTS

N.S.S. would like to acknowledge financial support from the Council of Science and Industrial Research (CSIR), India. G.S.S. and N.S.S. greatly acknowledge the Department of Science and Technology (DST)-SERB-ECR [ECR/2016/000203]. The authors would like to thank the Sophisticated Test and Instrumentation Centre (STIC), Cochin University of Science and Technology (CUSAT), Kerala, India for extending characterization facilities, the Department of Physics, CUSAT for FESEM analysis, and the CSIR-National Institute for Interdisciplinary Science and Technology (CSIR-NIIST), Trivandrum, Kerala, India for PPMS analysis.

■ ABBREVIATIONS

CI, crystallinity index; DAPI, 4′,6-diamino-2-phenylindole; DOX, doxorubicin; DMEM, Dulbecco's modified Eagle medium; DMSO, dimethyl sulfoxide; DNA, deoxyribonucleotide; DTG, derivative thermogram; FBS, fetal bovine serum; FDA, fluorescein diacetate; HOS, human osteosarcoma; MTT, 3-(4,5-dimethylthiazol-2-yl)-2,5-diphenyltetrazolium bromide; PBS, phosphate-buffered saline; PI, propidium iodide; PVA, polyvinyl alcohol; SPIONs, superparamagnetic iron oxide nanoparticles

■ REFERENCES

(1) Bee, S.; Banerjee, A.; Önyüksel, H. Improvement of Drug Safety by the Use of Lipid-Based Nanocarriers. *J. Controlled Release* **2012**, *163*, 34−45.

(2) Vassal, G.; Pondarre, C.; Boland, I.; Cappelli, C.; Santos, A.; Thomas, C.; Lucchi, E.; lmadalou, K.; Pein, F.; Morizet, J.; Gouyetle, A. Preclinical Development of Camptothecin Derivatives and Clinical Trials in Pediatric Oncology. *Biochimie* **1998**, *80*, 271−280.

(3) Lee, E.; Lee, J.; Jon, S. A Novel Approach to Oral Delivery of Insulin by Conjugating with Low Molecular Weight Chitosan. *Bioconjugate Chem.* **2010**, *21*, 1720−1723.

(4) Fang, C.; Kievit, F. M.; Cho, Y. C.; Mok, H.; Press, O. W.; Zhang, M. Effect of Cationic Side-Chains on Intracellular Delivery

and Cytotoxicity of PH Sensitive Polymer-Doxorubicin Nanocarriers. *Nanoscale* **2012**, *4*, 7012−7020.
(5) Unsoy, G.; Khodadust, R.; Yalcin, S.; Mutlu, P.; Gunduz, U. Synthesis of Doxorubicin Loaded Magnetic Chitosan Nanoparticles for PH Responsive Targeted Drug Delivery. *Eur. J. Pharm. Sci.* **2014**, *62*, 243−250.
(6) Ganguly, K.; Aminabhavi, T. M.; Kulkarni, A. R. Colon Targeting of 5-Fluorouracil Using Polyethylene Glycol Cross-Linked Chitosan Microspheres Enteric Coated with Cellulose Acetate Phthalate. *Ind. Eng. Chem. Res.* **2011**, *50*, 11797−11807.
(7) Li, H.; Jiang, F.; Ye, S.; Wu, Y.; Zhu, K.; Wang, D. Bioactive Apatite Incorporated Alginate Microspheres with Sustained Drug-Delivery for Bone Regeneration Application. *Mater. Sci. Eng., C* **2016**, *62*, 779−786.
(8) Diefenbeck, M.; Mückley, T.; Hofmann, G. O. Prophylaxis and Treatment of Implant-Related Infections by Local Application of Antibiotics. *Injury* **2006**, *37*, S95−S104.
(9) Yang, J.; Luo, L.; Oh, Y.; Meng, T.; Chai, G.; Xia, S.; Emmert, D.; Wang, B.; Eberhart, C. G.; Lee, S.; Stark, W. J.; Ensign, L. M.; Hanes, J.; Xu, Q. Sunitinib Malate-Loaded Biodegradable Microspheres for the Prevention of Corneal Neovascularization in Rats. *J. Controlled Release* **2020**, *327*, 456−466.
(10) Mao, X.; Li, X.; Zhang, W.; Yuan, L.; Deng, L.; Ge, L.; Mu, C.; Li, D. Development of Microspheres Based on Thiol-Modified Sodium Alginate for Intestinal-Targeted Drug Delivery. *ACS Appl. Bio Mater.* **2019**, *2*, 5810−5818.
(11) Jyoti, K.; Shankar, R.; Kush, P.; Kaushik, D.; Kumar, U.; Madan, J. Inhalable Bioresponsive Chitosan Microspheres of Doxorubicin and Soluble Curcumin Augmented Drug Delivery in Lung Cancer Cells. *Int. J. Biol. Macromol.* **2017**, *98*, 50−58.
(12) Yang, B.; Jiang, J.; Jiang, L.; Zheng, P.; Wang, F.; Zhou, Y.; Chen, Z.; Li, M.; Lian, M.; Tang, S.; Liu, X.; Peng, H.; Wang, Q. Chitosan Mediated Solid Lipid Nanoparticles for Enhanced Liver Delivery of Zedoary Turmeric Oil in Vivo. *Int. J. Biol. Macromol.* **2020**, *149*, 108−115.
(13) Xie, P.; Liu, P. PH-Responsive Surface Charge Reversal Carboxymethyl Chitosan-Based Drug Delivery System for PH and Reduction Dual-Responsive Triggered DOX Release. *Carbohydr. Polym.* **2020**, *236*, 116093.
(14) Kankala, R. K.; Liu, C. G.; Yang, D. Y.; Wang, S. B.; Chen, A. Z. Ultrasmall Platinum Nanoparticles Enable Deep Tumor Penetration and Synergistic Therapeutic Abilities through Free Radical Species-Assisted Catalysis to Combat Cancer Multidrug Resistance. *Chem. Eng. J.* **2020**, *383*, 123138.
(15) Khademi, Z.; Lavaee, P.; Ramezani, M.; Alibolandi, M.; Abnous, K.; Taghdisi, S. M. Co-Delivery of Doxorubicin and Aptamer against Forkhead Box M1 Using Chitosan-Gold Nanoparticles Coated with Nucleolin Aptamer for Synergistic Treatment of Cancer Cells. *Carbohydr. Polym.* **2020**, *248*, 116735.
(16) Kurmi, B. D.; Paliwal, R.; Paliwal, S. R. Dual Cancer Targeting Using Estrogen Functionalized Chitosan Nanoparticles Loaded with Doxorubicin-Estrone Conjugate: A Quality by Design Approach. *Int. J. Biol. Macromol.* **2020**, *164*, 2881−2894.
(17) Vo, N. T. N.; Huang, L.; Novakovic, L. H. M. A. Poly (Ethylene Glycol) -Interpenetrated Genipin-Crosslinked Chitosan Hydrogels : Structure , PH Responsiveness , Gelation Kinetics , and Rheology. *J. Appl. Polym. Sci.* **2020**, No. e49259.
(18) Carrefio-gmez, B.; Duncan, R. Evaluation of the Biological Properties of Soluble Chitosan and Chitosan Microspheres. *Int. J. Pharm.* **1997**, *148*, 231−240.
(19) Lai, J. Biocompatibility of Genipin and Glutaraldehyde Cross-Linked Chitosan Materials in the Anterior Chamber of the Eye. *Int. J. Mol. Sci.* **2012**, *13*, 10970−10985.
(20) Van Duong, H.; The, T.; Chau, L.; Thi, N.; Dang, T.; Vanterpool, F.; Salmero, M. Biocompatible Chitosan-Functionalized Upconverting Nanocomposites. *ACS Omega* **2018**, *3*, 86−95.
(21) Wang, L.; Stegemann, J. P. Glyoxal Crosslinking of Cell-Seeded Chitosan/Collagen Hydrogels for Bone Regeneration. *Acta Biomater.* **2011**, *7*, 2410−2417.
(22) Thong, Q. X.; Biabanikhankahdani, R.; Ho, K. L.; Alitheen, N. B.; Tan, W. S. Thermally-Responsive Virus-like Particle for Targeted Delivery of Cancer Drug. *Sci. Rep.* **2019**, *9*, 3945.
(23) Kashyap, S.; Singh, N.; Surnar, B.; Jayakannan, M. Enzyme and Thermal Dual Responsive Amphiphilic Polymer Core − Shell Nanoparticle for Doxorubicin Delivery to Cancer Cells. *Biomacromolecules* **2016**, *17*, 384−398.
(24) Liu, D.-D.; Wang, Y.; Han, G.-H. Synthesis of Carboxylated Silicon Phthalocyanine Photosensitive Microspheres with Controllable Etching. *Des. Monomers Polym.* **2019**, *22*, 98−105.
(25) Jeddi, M. K.; Mahkam, M. Magnetic Nano Carboxymethyl Cellulose-Alginate / Chitosan Hydrogel Beads as Biodegradable Devices for Controlled Drug Delivery. *Int. J. Biol. Macromol.* **2019**, *135*, 829−838.
(26) Cai, Q.; Yang, D.; Zhong, L.; Yang, P. A PH-Activable Chemo-Photodynamic Therapy Based on Cube-Wrapped-Cube α-NaYbF4:Tm@CaF2/Nd@ZnO Nanoparticles Mediated by 808 Nm Light. *Chem. Mater.* **2020**, *32*, 7492−7506.
(27) Wang, Z.; Zhu, H.; He, F.; Yan, D.; Jia, T.; Sun, Q.; Wang, X.; Wang, X.; Yang, D.; Gai, S.; Yang, P. Layer Structured LDH_ZnPcG4-FA Nanoplatform for Targeted and Imaging Guided Chemo-Photodynamic Therapy Mediated by 650 nm Light. *Chem. Eng. J.* **2020**, *382*, 122847.
(28) Xu, M.; Yang, G.; Bi, H.; Xu, J.; Dong, S.; Jia, T.; Wang, Z.; Zhao, R.; Sun, Q.; Gai, S.; He, F.; Yang, D.; Yang, P. An Intelligent Nanoplatform for Imaging-Guided Photodynamic/Photothermal/Chemo-Therapy Based on Upconversion Nanoparticles and CuS Integrated Black Phosphorus. *Chem. Eng. J.* **2020**, *382*, 122822.
(29) Zahn, D.; Weidner, A.; Saatchi, K.; Dutz, S. Biodegradable Magnetic Microspheres for Drug Targeting , Temperature Controlled Drug Release, and Hyperthermia. *Curr. Dir. Biomed. Eng.* **2019**, *5*, 161−164.
(30) Enriquez, G. G.; Rizvi, S. A.; D'Souza, M. J.; Do, D. P. Formulation and Evaluation of Drug-Loaded Targeted Magnetic Microspheres for Cancer Therapy. *Int. J. Nanomed.* **2013**, *8*, 1393−1402.
(31) Sheryl, C. J.; Philip, A.; Samrot, A. V. Synthesis and Characterization of Superparamagnetic Iron-Oxide Nanoparticles (SPIONs) and Utilization of SPIONs in X-Ray Imaging. *Appl. Nanosci.* **2017**, *7*, 463−475.
(32) Hu, S.-H.; Liu, T.-Y.; Liu, D.-M.; Chen, S.-Y. Nano-Ferrosponges for Controlled Drug Release. *J. Controlled Release* **2007**, *121*, 181−189.
(33) Lin, S. T.; Chou, H. C.; Chen, Y. W.; Chan, H. L. Redox-Proteomic Analysis of Doxorubicin-Induced Altered Thiol Activity in Cardiomyocytes. *Mol. BioSyst.* **2013**, *9*, 447−456.
(34) Gibaud, S.; Andreux, J. P.; Weingarten, C.; Renard, M.; Couvreur, P. Increased Bone Marrow Toxicity of Doxorubicin Bound to Nanoparticles. *Eur. J. Cancer* **1994**, *30*, 820−826.
(35) El-sayyad, H. I.; Ismail, M. F.; Shalaby, F. M.; Abou-el-magd, R. F.; Gaur, R. L. Histopathological Effects of Cisplatin , Doxorubicin and 5-Flurouracil (5-FU) on the Liver of Male Albino Rats. *Int. J. Biol. Sci.* **2009**, *5*, 466−473.
(36) Ananjana, K.; Swetha, S.; Prabha, P.; Nishad, K. V.; Manoj, K.; Balagopal, N. N.; Sailaja, G. S. Amino Acid Inspired Tunable Superparamagnetic Iron Oxide (SPION) Nanostructures with High Magnetic Hyperthermia Potential for Biofunctional Applications. *New J. Chem.* **2020**, *44*, 1962−1970.
(37) Wei, H.; Zhang, X.; Cheng, C.; Cheng, S. X.; Zhuo, R. X. Self-Assembled , Thermosensitive Micelles of a Star Block Copolymer Based on PMMA and PNIPAAm for Controlled Drug Delivery. *Biomaterials* **2007**, *28*, 99−107.
(38) Redol, E.; Desii, A.; Sartini, S.; La Motta, C.; Mazzolai, B.; Mattoli, V. PMMA/Polysaccharides Nano Film Loaded with Adenosine Deaminase Inhibitor for Targeted Anti-in Fl Ammatory Drug Delivery. *Langmuir* **2013**, *29*, 13190−13197.
(39) Genina, N.; Holländer, J.; Jukarainen, H.; Mäkilä, E.; Salonen, J.; Sandler, N. Ethylene Vinyl Acetate (EVA) as a New Drug Carrier

for 3D Printed Medical Drug Delivery Devices. *Eur. J. Pharm. Sci.* **2016**, *90*, 53−63.
(40) Julkapli, N. M.; Ahmad, Z.; Akil, H.; Julkapli, N. M.; Ahmad, Z. X-Ray Diffraction Studies of Cross Linked Chitosan With Different Cross Linking Agents For Waste Water Treatment Application. *AIP Conf. Proc.* **2010**, *1202*, 106−111.
(41) Schott, H. Kinetics of Swelling of Polymers and Their Gels. *J. Pharm. Sci.* **1992**, *81*, 467−470.
(42) Gupta, K. C.; Jabrail, F. H. Glutaraldehyde and Glyoxal Cross-Linked Chitosan Microspheres for Controlled Delivery of Centchroman. *Carbohydr. Res.* **2006**, *341*, 744−756.
(43) Grabska-Zielińska, S.; Sionkowska, A.; Coelho, C. C.; Monteiro, F. J. Silk Fibroin/Collagen/Chitosan Scaffolds Cross-Linked by a Glyoxal Solution as Biomaterials toward Bone Tissue Regeneration. *Materials* **2020**, *13*, 3433.
(44) Baran, T. New Chitosan-Glyoxal Beads Supported Pd(II) Catalyst: Synthesis, Characterization and Application in Suzuki Coupling Reactions. *Hacettepe J. Biol. Chem.* **2016**, *3*, 307−315.
(45) Li, B.; Shan, C. L.; Zhou, Q.; Fang, Y.; Wang, Y. L.; Xu, F.; Han, L. R.; Ibrahim, M.; Guo, L. B.; Xie, G. L.; Sun, G. C. Synthesis, Characterization, and Antibacterial Activity of Cross-Linked Chitosan-Glutaraldehyde. *Mar. Drugs* **2013**, *11*, 1534−1552.
(46) Yang, Q.; Dou, F.; Liang, B.; Shen, Q. Studies of Cross-Linking Reaction on Chitosan Fiber with Glyoxal. *Carbohydr. Polym.* **2005**, *59*, 205−210.
(47) Huang, J.; Deng, Y.; Ren, J.; Chen, G.; Wang, G.; Wang, F.; Wu, X. Novel *in situ* Forming Hydrogel Based on Xanthan and Chitosan Re-Gelifying in Liquids for Local Drug Delivery. *Carbohydr. Polym.* **2018**, *186*, 54−63.
(48) Zhou, X.; Li, Y.; Chen, S.; Fu, Y. n.; Wang, S.; Li, G.; Tao, L.; Wei, Y.; Wang, X.; Liang, J. F. Dynamic Agent of an Injectable and Self-Healing Drug-Loaded Hydrogel for Embolization Therapy. *Colloids Surf., B* **2018**, *172*, 601−607.
(49) Ding, F.; Shi, X.; Wu, S.; Liu, X.; Deng, H.; Du, Y.; Li, H. Flexible Polysaccharide Hydrogel with PH-Regulated Recovery of Self-Healing and Mechanical Properties. *Macromol. Mater. Eng.* **2017**, *302*, 1700221.
(50) Qu, J.; Liu, G.; Wang, Y.; Hong, R. Preparation of Fe_3O_4 − Chitosan Nanoparticles Used for Hyperthermia. *Adv. Power Technol.* **2010**, *21*, 461−467.
(51) Ioelovich, M. Crystallinity and Hydrophility of Chitin and Chitosan Crystallinity and Hydrophility of Chitin and Chitosan. *Res. Rev.: J. Chem.* **2014**, *3*, 7−14. e-ISSN: 2319-9849
(52) Yang, Q.; Dou, F.; Liang, B.; Shen, Q. Investigations of the Effects of Glyoxal Cross-Linking on the Structure and Properties of Chitosan Fiber. *Carbohydr. Polym.* **2005**, *61*, 393−398.
(53) Peng, H.; Wang, H.; Wu, J.; Meng, G.; Wang, Y.; Shi, Y.; Liu, Z.; Guo, X. Preparation of Superhydrophobic Magnetic Cellulose Sponge for Removing Oil from Water. *Ind. Eng. Chem. Res.* **2016**, *55*, 832−838.
(54) Corazzari, I.; Nisticò, R.; Turci, F.; Faga, M. G.; Franzoso, F.; Tabasso, S.; Magnacca, G. Advanced Physico-Chemical Characterization of Chitosan by Means of TGA Coupled on-Line with FTIR and GCMS: Thermal Degradation and Water Adsorption Capacity. *Polym. Degrad. Stab.* **2015**, *112*, 1−9.
(55) Jianmei, W.; Xueying, W.; Yan, L.; Hongyu, S.; Chengmin, C.; Jianchun, W.; Zongjun, L.; Krishnaswamy, N. Preparation and Properties of Magnetic Polymer Microspheres. *Polymer* **2020**, *199*, 122569.
(56) Rodkate, N.; Rutnakornpituk, M. Multi-Responsive Magnetic Microsphere of Poly(N-Isopropylacrylamide)/Carboxymethylchitosan Hydrogel for Drug Controlled Release. *Carbohydr. Polym.* **2016**, *151*, 251−259.
(57) Yuan, Y.; Chesnutt, B. M.; Utturkar, G.; Haggard, W. O.; Yang, Y.; Ong, J. L.; Bumgardner, J. D. The Effect of Cross-Linking of Chitosan Microspheres with Genipin on Protein Release. *Carbohydr. Polym.* **2007**, *68*, 561−567.
(58) Yin, Y.; Lv, X.; Tu, H.; Xu, S.; Zheng, H. Preparation and Swelling Kinetics of PH-Sensitive Photocrosslinked Hydrogel Based on Carboxymethyl Chitosan. *J. Polym. Res.* **2010**, *17*, 471−479.
(59) Wada, R.; Hyon, S. H.; Ikada, Y. Kinetics of Diffusion-Mediated Drug Release Enhanced by Matrix Degradation. *J. Controlled Release* **1995**, *37*, 151−160.
(60) Soares, J. S.; Zunino, P. A Mixture Model for Water Uptake, Degradation, Erosion and Drug Release from Polydisperse Polymeric Networks. *Biomaterials* **2010**, *31*, 3032−3042.
(61) Liu, L.; Liu, C.; Zhang, H.; He, J.; Zhai, J.; Yu, D.; Dong, S. How to Identify the " LIVE/DEAD " States of Microbes Related to Biosensing. *ACS Sens.* **2020**, *5*, 258−264.
(62) Simon, C.; Caorsi, V.; Sykes, C. Interplay between Membrane Tension and the Actin Cytoskeleton Determines Shape Changes. *Phys. Biol.* **2018**, *15*, No. 065004.
(63) Ge, Y.; Song, X.; Chen, L.; Hu, D.; Hua, L.; Cui, Y.; Liu, J.; An, Z.; Yin, Z.; Ning, H. Cadmium Induces Actin Cytoskeleton Alterations and Dysfunction in Neuro-2a Cells. *Environ. Toxicol.* **2019**, 469−475.
(64) Yin, T.; Liu, Y.; Yang, M.; Wang, L.; Zhou, J.; Huo, M. Novel Chitosan Derivatives with Reversible Cationization and Hydrophobicization for Tumor Cytoplasm-Specific Burst Co-Delivery of SiRNA and Chemotherapeutics. *ACS Appl. Mater. Interfaces* **2020**, *12*, 14770−14783.
(65) Rim, M. A.; Choi, J. H.; Park, A.; Youn, J.; Lee, S.; Kim, N. E.; Song, J. E.; Khang, G. Characterization of Gelatin/Gellan Gum/Glycol Chitosan Ternary Hydrogel for Retinal Pigment Epithelial Tissue Reconstruction Materials. *ACS Appl. Bio Mater.* **2020**, *3*, 6079−6087.
(66) Islam, N.; Dmour, I.; Taha, M. O. Degradability of Chitosan Micro/Nanoparticles for Pulmonary Drug Delivery. *Heliyon* **2019**, *5*, No. e01684.
(67) Singh, B. N.; Veeresh, V.; Mallick, S. P.; Jain, Y.; Sinha, S.; Rastogi, A.; Srivastava, P. Design and Evaluation of Chitosan/Chondroitin Sulfate/Nano-Bioglass Based Composite Scaffold for Bone Tissue Engineering. *Int. J. Biol. Macromol.* **2019**, *133*, 817−830.
(68) Garcia, A. R.; Lacko, C.; Snyder, C.; Bohórquez, A. C.; Schmidt, C. E.; Rinaldi, C. Processing-Size Correlations in the Preparation of Magnetic Alginate Microspheres through Emulsification and Ionic Crosslinking. *Colloids Surf., A* **2017**, *529*, 119−127.
(69) Lemaire, V.; Bélair, J.; Hildgen, P. Structural Modeling of Drug Release from Biodegradable Porous Matrices Based on a Combined Diffusion/Erosion Process. *Int. J. Pharm.* **2003**, *258*, 95−107.

https://doi.org/10.1021/acsomega.1c02303
ACS Omega 2021, 6, 21472−21484